J. Synchrotron Rad. (1997). **4**, 287–297

Protein Crystallography at Ultra-Short Wavelengths: Feasibility Study of Anomalous-Dispersion Experiments at the Xenon *K*-edge

Marc Schiltz,[a]* Åke Kvick,[b] Olof S. Svensson,[b] William Shepard,[a] Eric de La Fortelle,[c] Thierry Prangé,[a,d] Richard Kahn,[b,e] Gérard Bricogne[a,c] and Roger Fourme[a]

[a]LURE, Université de Paris-Sud, Bâtiment 209d, 91405 Orsay CEDEX, France, [b]ESRF, BP 220, 38043 Grenoble CEDEX, France, [c]MRC Laboratory of Molecular Biology, Hills Road, Cambridge CB2 2QH, UK, [d]Chimie Structurale Biomoléculaire, URA 1430 CNRS, UFR Biomédicale, 74 Rue M. Cachin, 93012 Bobigny CEDEX, France, and [e]Institut de Biologie Structurale Jean-Pierre Ebel, 41 Avenue des Martyrs, 38027 Grenoble CEDEX, France. E-mail: schiltz@lure.u-psud.fr

(*Received 4 February 1997; accepted 9 June 1997*)

A protein crystallography experiment at the xenon *K*-edge ($\lambda = 0.358$ Å) has been successfully carried out at the materials science beamline (BL2/ID11) of the ESRF. The samples used in this methodological study were crystals of porcine pancreatic elastase, a 26 kDa protein of known structure. The diffraction data are of excellent quality. The combination of isomorphous replacement and anomalous dispersion of a single xenon heavy-atom derivative allowed accurate phase determination and the computation of a high-quality electron density map of the protein molecule. This is the first fully documented report on a complete protein crystallography experiment, from data collection up to phase determination and calculation of an electron density map, carried out with data obtained at ultra-short wavelengths. Experimental considerations as well as possible advantages and drawbacks of protein crystallography at very short and ultra-short wavelengths are discussed.

Keywords: macromolecular crystallography; ultra-short-wavelength X-rays; data collection; anomalous dispersion; isomorphous replacement; xenon derivatives; radiation damage.

1. Theoretical background and scientific motivation

The potential benefits of using short-wavelength X-rays for protein crystallography have been examined by Arndt (1984). In particular, the systematic errors in the intensity measurements due to absorption become less severe and radiation damage is reduced. On second-generation synchrotrons, experimental stations dedicated to protein crystallography are usually operated at wavelengths in the range 0.9–1.1 Å for a number of reasons: (i) the maximization of the absorption efficiency of photographic film as the detector (Br *K*-edge at 0.92 Å), (ii) the maximization of the incident flux with insertion devices (at LURE-DCI and Daresbury-SRS the critical wavelengths of the wiggler emission curves are situated between 1.1 and 0.9 Å), and (iii) the possibility of optimized anomalous-scattering experiments with commonly used heavy atoms (Hg and Pt L_{III} edges) (Baker *et al.*, 1990). Although no exact comparative study has been carried out, the experience accumulated at these stations clearly indicates the superior quality of data collected at 0.9 Å as compared with Cu $K\alpha$ radiation ($\lambda = 1.54$ Å). The rationale behind this observation can be summarized as follows. The intensity of an integrated diffraction spot varies approximately as λ^2 (if due allowance is made for the Lorentz correction in rotation geometry) whereas photoelectric absorption cross sections vary as λ^3 (in between absorption edges). Thus, the ratio of diffracted over absorbed photons varies approximately as λ^{-1}. At short wavelengths systematic errors in the intensity measurements due to absorption can therefore be diminished. There is also much anecdotal evidence for increased sample lifetimes at 0.9 Å as compared with Cu $K\alpha$ wavelengths (Helliwell, 1992), although the theoretical reasons for these observations are less clear. At shorter wavelengths the number of photons deposited in the crystal by photoelectric absorption per scattered photon decreases, but the absorbed photons have a greater energy. Thus, in the wavelength range 0.5–1.5 Å, the energy absorbed per scattered photon is approximately independent of the wavelength (Arndt, 1984). Since it is not known whether radiation damage in the crystal follows the energy dose absorbed or the number of absorbed photons, the effect of short-wavelength X-rays on the sample lifetime remains uncertain. At very short

wavelengths (shorter than 0.5 Å) additional energy is deposited in the crystal due to the Compton effect (Nave, 1995).

Insertion devices installed on third-generation synchrotrons such as ESRF, APS or SPRING-8 provide high fluxes of narrowly collimated X-ray beams at very short† and ultra-short wavelengths up to ~0.15 Å. The use of very short wavelengths for protein crystallography experiments at these synchrotron sources was first advocated by Helliwell & Fourme (1983). A detailed theoretical analysis of the benefits of using very short and ultra-short wavelengths in protein crystallography has been given by Helliwell (1992) and Helliwell *et al.* (1993). These studies suggest that the decrease in sample absorption would give rise to several advantages: (i) the enhancement of high-resolution reflections and, as a direct consequence, the reduction of the overall temperature factor, (ii) the improvement of data accuracy due to reduced sample-to-sample variations in absorption, and (iii) the increase of sample lifetime.

There have been very few studies aimed at establishing whether these potential advantages make any difference in an actual diffraction experiment. Helliwell *et al.* (1993) have demonstrated the feasibility of collecting data frames on a lysozyme crystal at wavelengths of 0.5 and 0.3 Å with radiation produced by a 24-pole multipole wiggler at CHESS. Another pilot study was carried out by Gonzales, Denny & Nave (1994), who compared the quality of data and the relative background level in diffraction patterns obtained on a lysozyme sample at wavelengths of 0.92 and 0.55 Å on the SRS-Daresbury Wiggler Beamline 9.5. It has been argued (Helliwell, 1992; Helliwell *et al.*, 1993) that, at very short wavelengths, the detector can be moved further from the crystal for a given resolution limit and that an improvement in the signal-to-noise ratio of intensity measurements can be achieved in this way. The background on a diffraction image that arises from scattering processes (elastic as well as inelastic) is more or less smoothly distributed in space and hence falls off as d^2, where d is the crystal-to-detector distance. On the other hand, the size of the diffraction spots, because of the sharp beam collimation (low divergence of the incident beam for synchrotron radiation), remains constant. At a *fixed wavelength*, an increase in the crystal-to-detector distance will therefore lead to a reduction (by $1/d^2$) in the signal-to-background level (ignoring detector noise, which is independent of d). If, however, the wavelength is changed at the same time as the crystal-to-detector distance, the argument no longer holds for the contribution to the background arising from diffuse scattering as was recognized by Helliwell (1992) and Helliwell *et al.* (1993) [see Fig. 3 of Helliwell *et al.* (1993)]. It is also invalid for the background contributions arising from other elastic scattering processes, such as scattering from the capillary, the liquid and disordered solvent (Gonzales *et al.*, 1994). At shorter wavelengths these background components are compressed, in scattering angle, to the same extent as the Bragg diffraction. Since in standard diffraction experiments with protein crystals the background is often dominated by elastic scattering processes (if imaging plates with large oscillation angles are used) or by detector noise (if CCD detectors with small oscillation angles are used), no improvement in the signal-to-noise ratio is to be expected by reducing the wavelength. Thus, at the shorter wavelength of 0.55 Å Gonzales *et al.* (1994) did not observe any significant reduction in the spot-to-background intensity, as compared with at the wavelength of 0.92 Å.

Exact comparative studies at different wavelengths require the experimental conditions at the various wavelengths to be as similar as possible. This is very difficult to achieve in practice. Even if the same experimental set-up is used for all experiments, the beam properties (incident flux, monochromaticity and spatial divergence), as well as the detector characteristics (detective quantum efficiency and point-spread function), always vary with wavelength. And even if the same crystal, in the same orientation, is used for the collection of data at various wavelengths, different reflections will satisfy the Bragg conditions (due to the variation of the curvature of the Ewald sphere). Hence, the data frames cannot be compared directly with each other as they do not contain the same diffraction information. Also, it must be emphasized that the optimum experimental conditions for protein crystallography vary with wavelength. As an example, for a given experiment an imaging-plate detector might be the best choice at 0.9 Å, whereas at 0.36 Å another type of detector would be preferable. This also underlines the fundamental difficulty of drawing firm conclusions from one single experiment. In protein crystallography the quality of diffraction data depends on numerous factors which are interrelated to each other, sometimes in a subtle manner. Thus, the use of X-rays of shorter wavelengths might bring about a major improvement in data quality for some experiments whereas this might only be marginal in other cases.

Our aim in stating these facts is not an attempt to invalidate comparative studies at different wavelengths such as those carried out by Gonzales *et al.* (1994). Rather, we wish to caution against the overinterpretation of results based on investigations carried out on *one* particular sample with *one* particular experimental set-up. After all, the general feeling that wavelengths around 0.9 Å are better suited than longer wavelengths for protein crystallography did not emerge from a detailed comparative study or from one single case study, but rather from the practical experience accumulated from various projects at a number of synchrotron laboratories. We believe that a similar approach is needed to assess the advantages and drawbacks of using very short and ultra-short wavelengths in protein crystallography. The present study is intended to be a step in that direction.

A diffraction experiment on protein crystals was successfully carried out at the xenon K-edge (λ = 0.358 Å). The

† We here adopt the nomenclature used by Helliwell, Ealick, Doing, Irving & Szebenyi (1993), who define very short wavelengths as being close to 0.5 Å in contrast to short (0.9 Å) and ultra-short (0.3 Å) wavelengths.

combination of isomorphous replacement and anomalous dispersion of a xenon heavy-atom derivative was used to determine the phases and to compute a high-quality electron density map of the protein molecule. This is the first detailed report on a complete protein crystallography experiment, from data collection up to phase determination and calculation of an electron density map, carried out with data obtained at ultra-short wavelengths. In the presentation we will emphasize practical issues, such as instrumentation and data collection, and discuss experimental configurations that may be considered for protein crystallography at very short and ultra-short wavelengths.

2. Experimental: a SIRAS test study at the xenon *K*-edge

2.1. *Introduction: xenon as a heavy atom and anomalous scatterer*

The use of xenon as a heavy atom for determining protein phases by the method of isomorphous replacement (Vitali, Robbins, Almo & Tilton, 1991) has been generalized at the LURE laboratory (Schiltz, Prangé & Fourme, 1994; Schiltz, 1997). Useful extensions to the method have been presented by Stowell *et al.* (1996) and Sauer, Schmidt & Kratky (1997). Xenon has been shown to give highly isomorphous derivatives for numerous proteins (Schoenborn, Watson & Kendrew, 1965; Schoenborn, 1965; Tilton, Kuntz & Petsko, 1984; Schiltz, Fourme, Broutin & Prangé, 1995; Schiltz, 1997; Prangé *et al.*, 1997), and it has now been used successfully as a heavy atom in the structure determinations of the human nuclear retinoid-X receptor RXR-α ligand binding domain (Bourguet, Ruff, Chambon, Gronemeyer & Moras, 1995), the molybdoenzyme DMSO reductase from *Rhodobacter spheroides* (Schindelin, Kisker, Hilton, Rajagopalan & Rees, 1996), the oligomerization domain of the cartilage oligomeric matrix protein (COMP) (Malashkevich, Kammerer, Efimov, Schulthess & Engel, 1996), Photosystem I from *Synechococcus elongatus* (Krauss *et al.*, 1996), the lipoamide dehydrogenase domain from the outer membrane protein P64k of *Neisseria meningitidis* (Pernot *et al.*, 1996; Li de la Sierra *et al.*, 1997) and the enzyme Urate-Oxidase (Colloc'h *et al.*, 1996, 1997). In addition, xenon exhibits interesting anomalous-scattering properties: *K*- and L_{III}-absorption edges are at wavelengths of 0.3584 and 2.5927 Å, respectively (energies 34.592 and 4.782 keV, respectively). On the short-wavelength side of the L_{III}-edge, anomalous-scattering experiments have been carried out successfully by Vitali *et al.* (1991) with Cu $K\alpha$ radiation from a rotating anode.

In the present study we have investigated whether anomalous-dispersion experiments at the short-wavelength side of the *K*-edge can be undertaken. The experiment was carried out on crystals of porcine pancreatic elastase (PPE), a protein of known structure, for which xenon derivatives (one single site per enzyme molecule) had already been characterized (Schiltz *et al.*, 1994, 1995). Phases have been calculated by the SIRAS (single isomorphous replacement with anomalous scattering) method, based on a single xenon derivative. With a molecular weight of 25.9 kDa for PPE and with an imaginary anomalous-dispersion factor (f'') of 3.5 at the xenon *K*-edge, the expected Bijvoet differences on intensities are in the range of 3.35% (at zero scattering angle) for a single fully occupied xenon site. Clearly, this is a small signal and this experiment is therefore ideally suited to test whether measurements at ultra-short wavelengths can be of high accuracy. This experiment bears much resemblance to an earlier study (Schiltz *et al.*, 1997) where highly accurate phases were obtained with the SIRAS method on a single PPE–krypton derivative at the high-energy side of the krypton *K*-edge (λ = 0.86 Å).

2.2. *Sample preparation*

Lyophilized PPE from SERVA Chemicals was used without further purification. Crystals of PPE were grown at 291 K in 0.05 *M* acetate buffer, pH = 5.5, by the batch method using Na_2SO_4 as crystallizing agent (Meyer, Radhakrishnan, Cole & Presta, 1986). Crystals are of prismatic shape and can attain dimensions of 1.3 mm. They belong to space group $P2_12_12_1$ with cell parameters a = 51.6, b = 57.9 and c = 75.3 Å. In general, the crystallographic b direction is coincident with the long axis of the crystals. The crystal used for the native (*i.e.* without xenon) data collection was of size 0.8 × 1.3 × 1.0 mm and was mounted in a sealed Lindeman tube with a small amount of buffer.

The crystal used for data collection under xenon gas pressure was of size 0.3 × 0.6 × 0.4 mm and was mounted in a sealed quartz capillary that was fitted to a specially designed pressure cell† (Schiltz *et al.*, 1994). The pressurization device was mounted on a standard Huber goniometer head, so that the rotation arcs could be used to pre-orient the crystallographic axes. Crystal mounting and pressurization under xenon gas proceeded as described by Schiltz *et al.* (1994). The crystal was maintained at a xenon gas pressure of 16 bar (1 bar = 10^5 Pa $\simeq$ 1 atm) during the whole data-collection process. Data collection started about 0.5 h after pressurization.

2.3. *Instrumentation*

X-ray data collection was carried out in April 1996 on the materials science beamline BL2/ID11 (Kvick & Wulff, 1992) at the ESRF, with the storage ring operated at an energy of 6 GeV and with circulating electron currents of up to 180 mA. The radiation for this beamline is produced by a 24-pole wiggler with a gap tuned to 20 mm, giving a critical energy of 29 keV. The beamline optical elements feature a Pt-coated Si premirror, a double-crystal monochromator installed with Si (111) crystals and a second Pt-coated mirror. This combination provides wavelength tunability in the energy range 7–100 keV with an energy resolution close

† A detailed description of this pressure cell can be found on the internet at the following address: http://www.lure.u-psud.fr/www/lure/sections/XENON/xenon_eng.html.

Table 1
X-ray data collection and processing.

	Native PPE		PPE–Xenon (16 bar)
	Pass 1	Pass 2	
Data collection			
Exposure time per frame (s)	25	10	15
Angular increment per frame (°)	0.5	0.5	0.25
Total rotation range (°)	100	100	100
Crystal-to-detector distance (mm)	255	405	255
Data reduction			
Number of measured reflections	186157	68966	84666
Number of unique reflections	44760		14848
Resolution limits (Å)	17.34–1.40		13.18–1.80
Data completeness (%)	96.5		70.0
R_{merge}†	0.036		0.049
R_{merge} for data up to 2.5 Å resolution	0.028		0.039
R_{merge} in the last resolution shell	0.28		0.23
$\langle I/\sigma(I)\rangle$	27.84		28.72

† R_{merge} is defined as $\sum_{h,k,l}\sum_i |\langle I(h,k,l)\rangle - I_i(h,k,l)|/\sum_{h,k,l}\sum_i I_i(h,k,l)$, where $I_i(h,k,l)$ is the ith observation of reflection h, k, l and $\langle I(h,k,l)\rangle$ is the weighted mean of all observations (after rejection of outliers).

to $\Delta E/E = 2 \times 10^{-4}$. Beam focusing in the horizontal plane can be achieved by sagittal bending of the second monochromator crystal, but this is only possible for energies up to about 30 keV. For this reason, all experiments described in this study have been carried out with an unfocused beam. Slits were used to limit the beam to a size of 0.3×0.3 mm^2.

In order to locate the *K*-edge of xenon (34.592 keV) precisely the monochromator crystals were moved in the 30 keV region and calibrated using the absorption of an Sb foil (*K*-edge at 30.491 keV). A dried quartz capillary was filled with xenon gas and pressurized at 15 bar. An energy scan in the 34 keV region with steps of 25 eV was performed on this sample. At each step the fluorescence of the sample was measured with an NaI scintillation detector. This allowed us to locate the xenon *K*-edge with an accuracy of 25 eV. The diffraction experiments were carried out at an energy of about 50 eV above (*i.e.* on the high-energy side) the *K*-edge.

The detector consisted of a Be-windowed X-ray image intensifier (XRII) coupled to a slow-scan CCD camera. This system has been developed by the ESRF detector group (Moy, 1994) and its performance in diffraction experiments has been evaluated by Bourgeois, Moy, Svensson & Kvick (1994) and by Hammersley *et al.* (1997). The main reason for this choice of detector system is its high absorption efficiency (compared with other detectors, such as imaging plates) at energies close to the xenon *K*-edge. This is essentially due to the presence of a CsI scintillator (see also Fig. 5 and the discussion in §3.2).

The detector was calibrated for non-uniformity of response, spatial distortions and variations of signal-independent background (dark counts) according to methods and procedures developed by Hammersley *et al.* (1995). These calibrations were performed just before or just after the actual diffraction experiments and under similar conditions (in particular, with the same sample-to-detector distance). Non-uniformity of response was evaluated *via* a 2θ scan with a photon-counting detector of the flood field produced by an isotropically emitting Ba-doped lithium tetraborate glass sample (Moy *et al.*, 1996). This calibration took place at the Ba *K*-edge ($\lambda = 0.331$ Å, $E = 37.451$ keV). Spatial distortion calibration was performed with a known spacing calibration grid (Hammersley *et al.*, 1997). Dark noise was evaluated by averaging a series of data frames that were obtained with the same exposure times as the actual diffraction frames but without incident beam.

2.4. *Data collection*

Details of the various data-collection runs are given in Table 1. All data were collected at a room temperature of 291–294 K. Two consecutive data collections were recorded on the randomly oriented native crystal. In a first pass the aim was to accurately record the weak high-resolution reflections by setting the detector close to the crystal and by using long exposure times. Because of this set-up a number of strong reflections at low resolution contained overloaded pixels and were subsequently rejected at the data-processing stage. The spindle was then brought back to its initial position and data were recollected in a second pass with reduced exposure times and at a longer crystal-to-detector distance. In this way the strong reflections (mainly at low resolution) could be recorded without saturation effects. A typical data frame is shown in Fig. 1. For the xenon derivative the crystal was pre-oriented so that the crystallographic *b* direction was exactly coincident with the spindle axis. This allowed for the simultaneous recording of Bijvoet pairs on the same frame. All derivative data were collected in a single pass, on a single crystal.

Some technical problems prevented the data from being collected under perfect conditions. (i) The incident beam was not centred on the detector midpoint (see Fig. 1). This

implies that the full active surface of the detector could not be used. (ii) The size and position of the beam-stop prevented the collection of very low resolution reflections. (iii) The goniometer central position was not perfectly coincident with the incident X-ray beam, which means that the crystals progressively moved somewhat out of the beam. Thus, the frames recorded at the end of each pass exhibited a significant reduction in signal strength and, consequently, some reduction of the data quality. There are no fundamental difficulties in overcoming these obstacles but, because of beamtime constraints, this could not be attempted here. In spite of these problems these diffraction experiments yielded high-quality data.

2.5. *Data processing*

The raw data frames were corrected for spatial distortions, non-uniformity of response and dark counts with the program *FIT2D* (Hammersley, Svensson & Thompson, 1994), based on the detector calibration described above. Data processing was carried out with *MOSFLM* (Leslie, 1992). Although this program was originally written for processing film and imaging-plate data, we found it to be very versatile and easily adaptable to the processing of *corrected* data frames from the XRII/CCD detector. Data reduction and merging were carried out with programs of the *CCP*4 (Collaborative Computational Project, Number 4, 1994) suite along lines indicated by Schiltz *et al.* (1997). The results are summarized in Table 1. The effective mosaic spread of the crystal was estimated by the post-refinement technique implemented in *MOSFLM* and refined to values of 0.10–0.15°. The quality of the data is illustrated in Fig. 2, which shows the internal agreement factor of symmetry-related reflections as a function of resolution for the native crystal. Because of the smaller crystal size and reduced incident beam intensity (due to absorption by pressurized xenon gas in the capillary†), useful data could only be obtained to a resolution of 1.8 Å for the xenon derivative. A second data-collection pass with prolonged exposure times would probably have yielded higher resolution data (at the expense of saturation effects for strong low-resolution reflections), but this was not performed here.

2.6. *Phase determination*

Isomorphous and anomalous difference Patterson maps were computed. In these maps the Harker vectors corresponding to the single xenon site feature prominently (Fig. 3). Heavy-atom refinement and phasing were carried out using *SHARP* (La Fortelle & Bricogne, 1997) along the lines indicated by Schiltz *et al.* (1997). Results are summarized in Table 2. Subsequently, the quality of the phases was improved by the density-modification procedure implemented in *SOLOMON* (Abrahams & Leslie, 1996). The weighted mean phase difference with respect to phases computed from the refined native structure is 30.7°. Detailed phasing statistics for the data before and after density modification are given in Table 3.

† The linear X-ray attenuation coefficient of xenon under normal conditions (temperature = 273.1 K, pressure = 1.013 bar) is μ_l° = 0.14 cm^{-1} for a wavelength just above the *K*-edge, on the high-energy side. This can be compared with corresponding values at λ = 0.9 Å (μ_l° = 0.42 cm^{-1}) and at the Cu $K\alpha$ wavelength (μ_l° = 1.8 cm^{-1}) [numerical data computed from experimental cross sections reported by Saloman, Hubbell & Scofield (1988)]. Under the conditions of the experiment (pressure = 16 bar), the linear attenuation coefficient of gaseous xenon is μ_l (p = 16 bar, λ = 0.358 Å) = 2.2 cm^{-1}. Thus, X-rays travelling through the pressurized xenon gas on a path length of 0.3–0.5 mm will be reduced in intensity by about 10%.

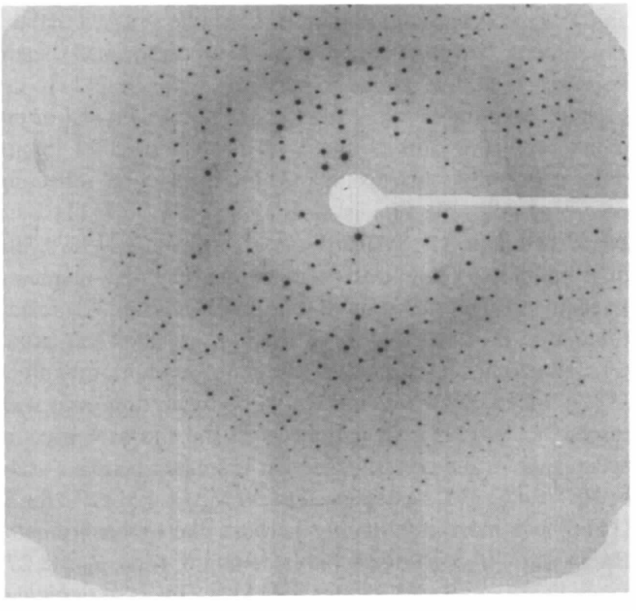

Figure 1
Data frame obtained at the Xe *K*-edge (λ = 0.358 Å) on a randomly oriented native crystal of PPE. Rotation angle: 0.5°. Exposure time: 10 s. Crystal-to-detector distance: 405 mm. ESRF beamline ID11 (BL2) illuminated by a 24-pole wiggler.

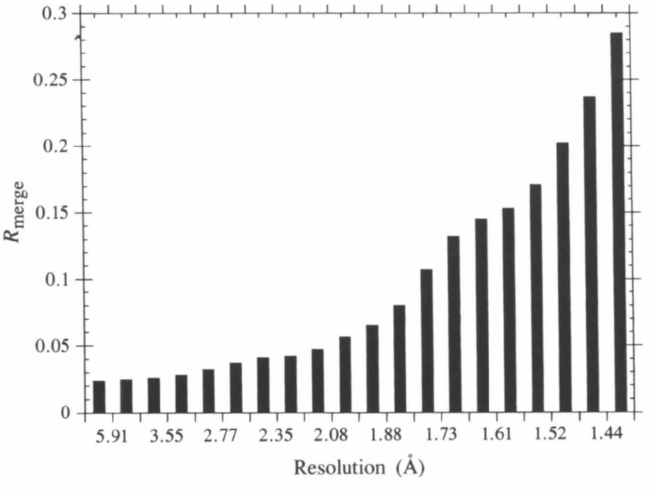

Figure 2
Quality of the native diffraction data: R_{merge} as a function of resolution. R_{merge} is defined as $\sum_{h,k,l} \sum_i |\langle I(h,k,l)\rangle - I_i(h,k,l)| / \sum_{h,k,l} \sum_i I_i(h,k,l)$, where $I_i(h,k,l)$ is the ith observation of reflection h,k,l and $\langle I(h,k,l)\rangle$ is the weighted mean of all observations (after rejection of outliers).

2.7. *Results*

Examples of the final electron density map at 1.8 Å resolution are shown in Fig. 4. The map is of high quality and is in very good agreement with the known protein structure: the map correlation coefficient between this map and a map calculated from the refined molecular structure of the protein is 0.80. The quality of the map (see also Table 3) is slightly inferior to that obtained from a similar experiment with krypton gas at the *K*-edge (λ = 0.86 Å) (Schiltz *et al.*, 1997). This can in part be attributed to the experimental problems outlined above. In particular, the lack of low-resolution reflections impaired the effectiveness of the density-modification strategy. Also, it must be stressed that in this study the native and derivative data were collected on two different crystals, thus giving rise to possible inter-crystal scaling errors and non-isomorphism. On the other hand, for the study with krypton gas, the same crystal in the same orientation was used for both the derivative and the native data collection.

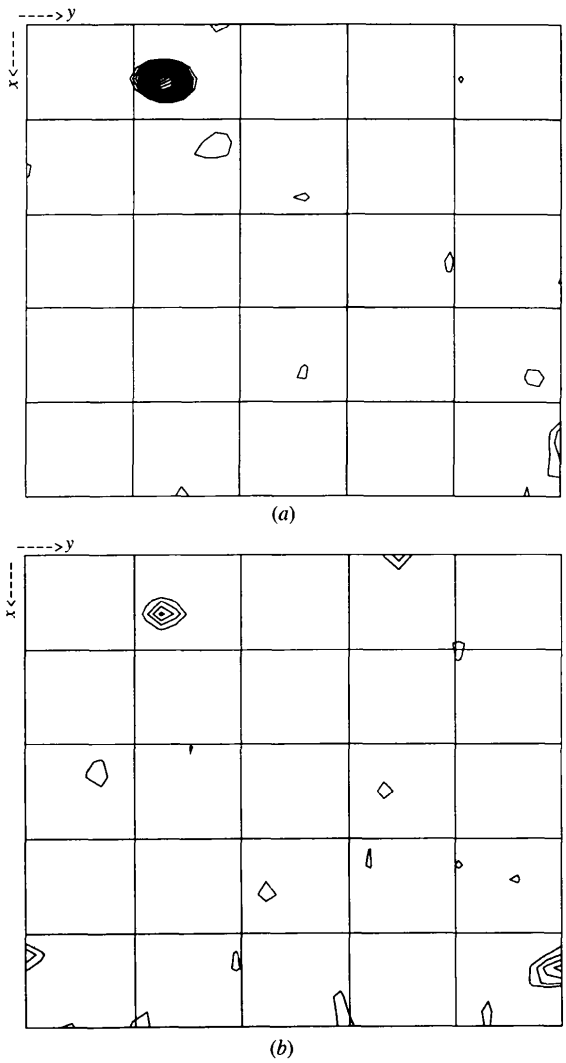

Figure 3
Isomorphous-difference (*a*) and anomalous-difference (*b*) Patterson maps. The asymmetric part ($0 \le x \le 0.5$, $0 \le y \le 0.5$) of the Harker sections $z = 0.5$ are shown. Contours are at intervals of 1σ, starting 2σ above the mean density (where σ is the root mean square of the map density). In both maps the interatomic Xe–Xe Harker vectors at $z = 0.5$ and $y = 0.5$ can be seen.

3. Discussion: protein crystallography at very short and ultra-short wavelengths

The experiment described above has demonstrated that protein crystallography at ultra-short wavelengths can provide highly accurate diffraction data. The weak anomalous signal of the Xe atom was successfully combined with the isomorphous signal to extract high-quality phase information. In this section we discuss some alternatives and improvements that can be considered for experiments at very short and ultra-short wavelengths

3.1. *X-ray source and beamline optics*

A major concern at ultra-short wavelengths is the reduced scattering efficiency of the sample. As indicated above, the scattering efficiency (in rotation geometry) varies approximately as λ^2. Hence, by shifting from λ = 0.9 to 0.36 Å, a more than sixfold reduction in diffracted intensities per incident X-ray photon is to be expected. This reduction in scattering efficiency, however, is compensated by the high incident fluxes produced with insertion devices at third-generation synchrotrons. In our experiments the exposure times were still shorter than or equal to 60 s per degree of rotation. This is only slightly greater than the exposure times needed with this same sample at λ = 0.9 Å on the LURE-DCI wiggler beamline DW32 (exposure times between 15 and 45 s per degree of rotation). It has to be stressed that the experiments were carried out with an unfocused beam. Focusing was not possible because, with Si (111), the sagittal curvature is too severe for the second crystal in the monochromator. This is, however, not the case for higher order reflections such as Si (331). The integral reflecting power of this reflection is smaller than for Si (111) by a factor of about 3.4 (Matsushita & Hashizume, 1983), but this would be more than compensated by the increased intensity brought about by line or point focusing. Exposure times would be reduced by at least an order of magnitude with respect to the present experiment. In addition, with Si (331), the energy resolution would be much improved with respect to Si (111), in part because the intrinsic spectral acceptance of the crystal reflection is smaller [$\Delta E/E = 1.44 \times 10^{-5}$ for Si (331) as opposed to $\Delta E/E = 1.4 \times 10^{-4}$ for Si (111)], but more importantly because the monochromator Bragg angle (θ_B) is larger† [at the xenon *K*-edge, $\theta_B = 8.27°$ for Si (331) and $\theta_B = 3.28°$ for Si (111)]. This is of particular importance if MAD (multiwavelength anomalous disper-

† The contribution to the energy resolution of a double-crystal monochromator that arises from the angular spread of the incident beam varies as cot θ_B (see Helliwell, 1992, p. 154).

Table 2
Heavy-atom parameter refinement.

One single Xe atom was refined.

Fractional coordinates	$(x, y, z) = (0.2805 \pm 0.0001; 0.0639 \pm 0.0001; 0.4883 \pm 0.0001)$
Occupancy	0.768 ± 0.009
Isotropic temperature factor (B_{iso})	(15.5 ± 0.3) Å^2
Anisotropic perturbations (tensor of b_{ij})†	$(-0.5 \pm 0.1; 0.5 \pm 0.1; 1.1 \pm 0.2; 0.4 \pm 0.2; 1.2 \pm 0.2; 0.1 \pm 0.3)$
Anomalous-scattering factors	$f' = -4.0$ (not refined); $f'' = 3.8 \pm 0.1$ (refined)‡

† The temperature factor of the Xe atom is modelled as the sum of an isotropic term (a diagonal matrix with elements B_{iso}) and an anisotropic perturbation (a tensor with elements b_{ij}); see also Schiltz *et al.* (1997). ‡ The occupancy of the heavy atom, and its imaginary and real dispersion corrections (f' and f''), cannot be refined independently as each parameter is linearly correlated with the two others. For this reason, f' was fixed at the theoretical value of -4.0 whereas the two other parameters were refined. In addition, f'' refines to a value slightly above what is expected from theoretical calculations ($f''_{theoretical} = 3.51$), possibly because the Xe atom replaces water molecules in the cavity (Schiltz *et al.*, 1997), so that the refined value for its occupancy underestimates the physical occupancy.

Table 3
Phasing statistics in resolution shells.

Heavy-atom refinement and phasing were carried out using *SHARP* (La Fortelle & Bricogne, 1997). Density modification was performed using *SOLOMON* (Abrahams & Leslie, 1996). ISO stands for isomorphous differences. ANO stands for anomalous differences. Isomorphous phasing power is defined as $\langle |\mathbf{F}_H| / \int_0^{2\pi} (|\mathbf{F}_{PH}| - |\mathbf{F}_P + \mathbf{F}_H|)\, d\varphi_P \rangle$, where $\mathbf{F}_H$ is the calculated heavy-atom structure factor, $\mathbf{F}_P$ is the protein structure factor with $\mathbf{F}_P = |\mathbf{F}_P| \exp(i\varphi_P)$ where $|\mathbf{F}_P|$ is the measured protein structure-factor amplitude and φ_P is the calculated phase angle. $|\mathbf{F}_{PH}|$ is the measured heavy-atom derivative structure-factor amplitude. Anomalous phasing power is defined as: $\langle |\mathbf{F}_H^+ - \mathbf{F}_H^-| / \int_0^{2\pi} [(|\mathbf{F}_{PH}^+| - |\mathbf{F}_{PH}^-|) - (|\mathbf{F}_P + \mathbf{F}_H^+| - |\mathbf{F}_P + \mathbf{F}_H^-|)]\, d\varphi_P$, where $|\mathbf{F}_{PH}^+| - |\mathbf{F}_{PH}^-|$ is the measured Bijvoet-difference of the heavy-atom-derivative structure-factor amplitude. $\mathbf{F}_H^+$ and $\mathbf{F}_H^-$ are the total calculated heavy-atom structure factors for both members of the Bijvoet pair. FOM is the mean figure of merit of the complex structure-factor probability distributions. $\langle \Delta\varphi \rangle$ is the mean phase difference (weighted by $|\mathbf{F}_P| \times$ FOM so as to optimally reflect the quality of the electron density map) with respect to phases calculated from the refined native protein structure. CORREL is the correlation coefficient between experimental and calculated (from the refined native protein structure) complex structure factors in reciprocal space (with statistical weights so as to be equivalent to a correlation coefficient in real space – by Parseval's theorem).

Resolution (Å)	**ALL**	50.0	5.07	3.59	2.94	2.54	2.28	2.08	1.92	1.80
Phasing power										
Centrosymmetric ISO	**2.20**		5.03	2.16	2.00	2.17	1.78	1.71	1.60	1.49
Acentric ISO	**2.70**		6.56	3.35	3.05	3.00	2.55	2.12	2.02	2.07
Non-centrosymmetric ANO	**0.96**		2.19	1.44	1.27	1.11	0.90	0.73	0.64	0.51
SIRAS phasing										
FOM	**0.32**		0.58	0.57	0.45	0.37	0.32	0.30	0.21	0.17
$\langle \Delta\varphi \rangle$	**58.7**		57.3	50.9	51.8	55.2	59.8	63.1	69.4	79.2
CORREL	**0.46**		0.41	0.53	0.53	0.48	0.42	0.39	0.30	0.19
SIRAS phasing and density modification										
FOM	**0.89**		0.85	0.91	0.90	0.89	0.90	0.91	0.89	0.88
$\langle \Delta\varphi \rangle$	**30.7**		37.4	25.8	30.5	31.3	30.4	29.4	31.8	33.4
CORREL	**0.80**		0.72	0.85	0.80	0.78	0.81	0.82	0.78	0.77

sion) experiments are to be performed, where the energy resolution needs to be close to or smaller than the natural width of the core level under investigation [the natural width of the K level for xenon is 11.4 eV (Krause & Oliver, 1979)]. In conclusion, with appropriate optics, exposure times of a few seconds per degree can be expected with high-quality samples (such as PPE crystals), whereas these will be on a timescale of a few minutes with weakly diffracting samples. At X-ray energies of ~30 keV, undulators as well as multipole wigglers can be considered as suitable sources.

3.2. *Detectors*

Among the devices currently available, two types of detectors can be considered for diffraction experiments at very short and ultra-short wavelengths: imaging plates and CCD-based detectors. Various imaging-plate systems as well as the Be-windowed XRII/slow-scan CCD system have been tested in terms of spatial resolution (point-spread function) and dynamic range at high X-ray energies by Bourgeois *et al.* (1994). Both systems give similar results, with the XRII/CCD having a somewhat larger dynamic range and the imaging plate, due to its larger size, being capable of recording more diffraction spots. Another important characteristic is the absorption efficiency (see Fig. 5). The absorption efficiency of BaFBr-coated imaging plates decreases rapidly at wavelengths shorter than 0.7 Å but the Ba K-edge enhances this again for wavelengths shorter than 0.331 Å. For the XRII/CCD detector a similar behaviour is observed, but the specific enhancement of the absorption efficiency occurs at the I and Cs K-edges (λ = 0.3738 and 0.3445 Å, respectively). It appears from this analysis that the choice of the optimum wavelength is

restricted to the 0.37–0.25 Å range where the detector absorption efficiency is maximized and where the incident X-ray fluxes are still large enough to allow fast data collection. Although the absorption efficiency as a function of wavelength is certainly the most important characteristic that has to be considered, it should be stressed that higher energy photons give more signal when absorbed, thereby overcoming any noise in the detector system. The image plates have been characterized in the literature for the signal obtained as a function of wavelength.

The choice of detector might also be dictated by more practical considerations. Imaging-plate systems with an integrated scanner are easy to use but the main drawback is their rather low duty cycle which limits the speed of data acquisition. The XRII/CCD detector that was used in this study had a readout time of 10 s per frame. The upgrading of this system by the faster camera that is currently being developed by the ESRF detector group will result in readout times on a sub-second timescale. As a major drawback, the XRII system suffers from various distortions that make a careful detector calibration mandatory (as described above). In principle, the calibration has to be repeated for each new experimental configuration and this can be rather time-consuming.

Fibre-optically coupled CCD detectors are easy to use and are versatile in the sense that the scintillation phosphor screen can easily be changed. This is, for instance, the case with the *SMART* system that is commercialized by Siemens, where different scintillation phosphors can be mounted in order to maximize the absorption efficiency either at the Cu $K\alpha$ or at the Mo $K\alpha$ wavelengths. Thus, it is conceivable that a number of suitable scintillation phosphors can be found that would enable CCD detectors to cover the whole range from Cu $K\alpha$ up to ultra-short wavelengths. Further research and development in this field would be most helpful.

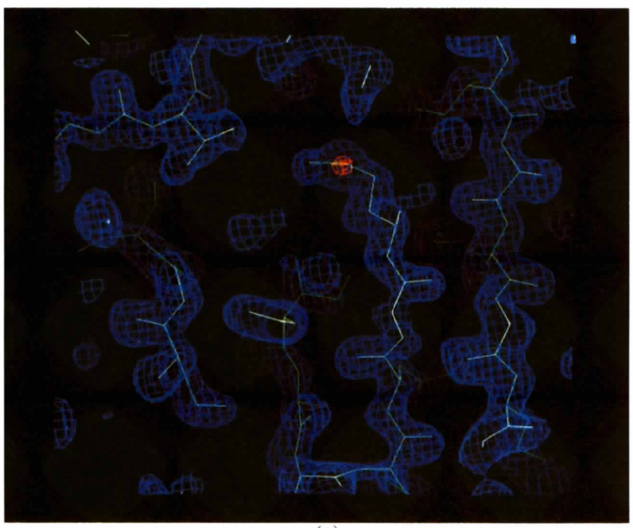

(*a*)

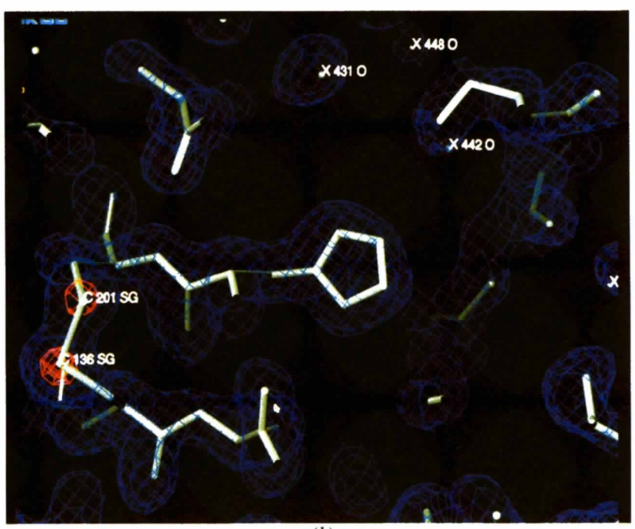

(*b*)

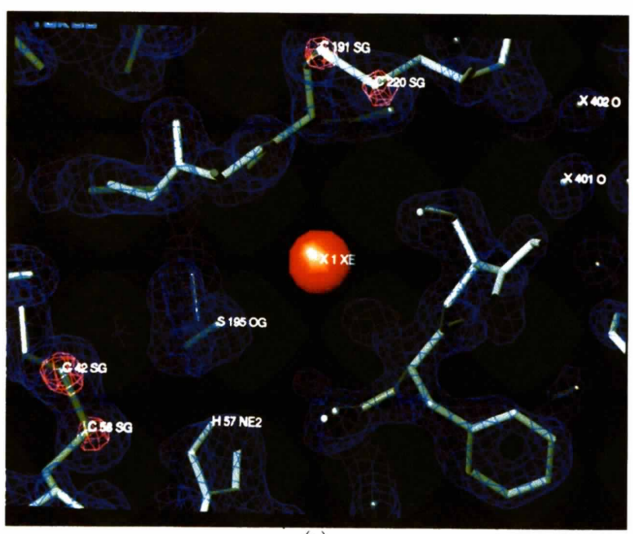

(*c*)

Figure 4
Representative views of the SIRAS electron density map at 1.8 Å resolution obtained with phases from *SHARP* and after density modification with the *SOLOMON* program. Contours are at 1.2σ (blue) and 7σ (red) above the mean density (where σ is the root mean square of the map density). Superimposed onto this map is the refined native structure of the PPE molecule (in green) as obtained from the Protein Data Bank at Brookhaven (entry: 1LVY). It should be noted that this electron density map was obtained from purely experimental data, *i.e.* prior to any model building. As can be seen, the agreement with the molecular model of the protein is very good. (*a*) Overall view of a β sheet. The red spherical density peak corresponds to a sulfur atom in a methionine residue. (*b*) Close-up view of the Cys-136—Cys-201 disulfide bridge. (*c*) Close-up view of the xenon binding site. The xenon atom is displayed as a red ball. Also shown are the Cys-42—Cys-58 and Cys-191—Cys-220 disulfide bridges, as well as the catalytic Ser-195 and His-57 residues. The quality of the map can be judged from the fact that refined water molecules show up as spherical density peaks [waters 431, 442 and 448 in (*b*) and waters 401 and 402 in (*c*)].

A final remark is in order concerning specifically the experiments at the xenon *K*-edge. From our previous work with krypton we have found that fluorescence from the pressurized gas in the capillary causes strong background noise on the diffraction frames (Schiltz *et al.*, 1997). These problems also arise with xenon gas. But since the absorption efficiency of the XRII/CCD system rises sharply at the I *K*-edge, the diffracted photons are detected with an efficiency that is much larger than that of the fluorescent photons, which have a longer wavelength (Xe $K\alpha$ line at 0.418 Å) and, hence, fall in the region where the absorption efficiency is minimal (see Fig. 5). For this experiment the detector has therefore proved to be an efficient discriminator between useful signal (diffracted beams) and fluorescence background.

3.3. *Data collection and data quality*

As indicated above, the data quality is quite satisfactory. In particular, we have been able to collect native data up to a maximum resolution of 1.4 Å. With this sample, usable data could only be recorded to a resolution limit of about 1.6 Å at a wavelength of 0.9 Å on the LURE-DCI wiggler beamline DW32. To what extent the increase in the resolution limit is due to the change in wavelength remains unclear,† but Helliwell (1992) and Helliwell *et al.* (1993) have suggested that the reduced absorption of X-rays would lead to an enhancement of the high-resolution reflections at very short and ultra-short wavelengths. The reduction of the reflection range for high-resolution reflections might also be of some importance. The reflection range depends on the X-ray beam divergence angles and on the spectral bandwidth. It increases with high Bragg angles due to the effect of spectral smearing. Since, at shorter wavelengths, the high-resolution reflections are scattered at lower Bragg angles, this effect of spectral smearing might be reduced. Finally, the obliquity of incidence of the diffracted beam onto the flat detector surface may also play a role. The size of a diffraction spot on a flat detector, mounted perpendicular to the direction of the incident X-ray beam, varies as $1/\cos 2\theta_B$, where θ_B is the Bragg angle of the reflection. Thus, the use of shorter wavelengths gives rise to sharper diffraction spots and hence to better statistics in the measurements, and this is particularly true for high-resolution reflections.‡ These considerations would suggest that the use of X-rays of very short and ultra-short wavelengths might be of particular interest for highly accurate high-resolution studies. In addition, the blind region is substantially reduced at short wavelengths so that complete data sets can be obtained with fewer data exposures.

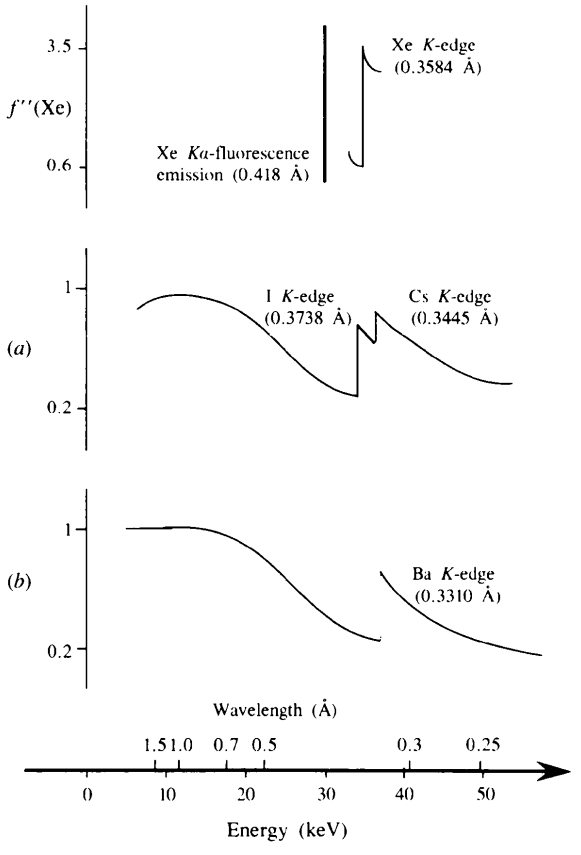

Figure 5
Schematic representation of the absorption efficiencies of (*a*) the Be-windowed XRII/slow-scan CCD detector and (*b*) the BaFBr imaging plate. These curves are not on a common absolute scale and are merely used for qualitative comparisons of absorption efficiencies as a function of wavelength. Exact quantitative analyses can be found in Amemiya (1990) and Moy (1994). Also shown are the xenon *K*-edge (imaginary anomalous-dispersion factor f'') and the xenon $K\alpha$-fluorescence emission line.

Background scattering due to the Compton effect increases with high Bragg angles, but, as was pointed out by Gonzales *et al.* (1994), if the detector is moved away from the sample to compensate for the change in wavelength, the Compton-background distribution will be the same for all wavelengths. Thus, although the total cross section for Compton scattering increases at short wavelengths (Nave, 1995), the Compton scattering at any Bragg resolution remains (to a first approximation) the same. There is therefore no reason for believing that increased background due to the Compton effect will occur at ultra-short wavelengths.

3.4. *Radiation damage*

Radiation damage in protein crystals is a rather complex phenomenon. A comprehensive treatment of this subject can be found in the review article by Nave (1995). As was indicated earlier, at constant diffracted intensity the energy dose deposited in the crystal by photoelectric absorption is

† The experimental conditions were not identical. In particular, the detector used at LURE is an image-plate system. The CCD system employed at the ESRF probably has a higher efficiency for weak data (which are mostly at high resolution).

‡ It must be pointed out that the background arising from scattering processes is also smeared out at higher angles (*i.e.* it also varies as $1/\cos 2\theta_B$), but not the detector readout noise and dark current. Thus, for a detector with low noise (such as gas detectors), no improvement due to a reduced obliquity of incidence is to be expected.

not likely to change very much with wavelength (Arndt, 1984; Nave, 1995). However, at X-ray energies above 30 keV the Compton effect becomes the predominant process and total incoherent scattering energy-absorption cross sections do increase quite rapidly at ultra-short wavelengths (Hubbell *et al.*, 1975). We believe that the limited results of the present study cannot establish whether the use of ultra-short-wavelength X-rays reduces radiation damage or not. We can only state that, in spite of the high incident flux and despite the fact that the experiment was carried out at room temperature, we did not notice unusually high radiation damage. Before data reduction the various frames were brought onto a common scale by applying overall and resolution-dependent (pseudo-temperature) scale factors. The resolution-dependent scale factor typically corrects intensity losses due to radiation damage. As an example, for the first pass of the native data collection this resolution-dependent scale factor varies monotonically from 0.0 (first frame) to 0.45 Å^2 (last frame). These are small values, which are comparable with results obtained at a wavelength of 0.9 Å, and they are indicative of the fact that radiation damage was not a serious issue. Whether this observation can be generalized remains to be elucidated by further studies.

It is well known that cryocooling greatly reduces radiation damage to the crystals. Although the present study was carried out at room temperature, it is possible to use the technique of cryocooling with krypton and xenon derivatives, as was first demonstrated by Schiltz *et al.* (1997). An elegant technique of performing flash-freezing on xenon derivatives in a simple manner is described by Sauer *et al.* (1997).

4. Conclusions

In this study it has been demonstrated that anomalous-scattering experiments at the xenon *K*-edge can be carried out successfully on protein crystals. The high fluxes available at third-generation synchrotrons allow protein crystallography experiments at very short and ultra-short wavelengths to be carried out fairly rapidly. A combination of beamline performance and adequate detector capabilities allowed us to obtain high-quality data that enabled us to calculate structure-factor phases for a 26 kDa protein from a single heavy-atom derivative. Clearly, this study has shown that there are no major obstacles to performing protein crystallography experiments at ultra-short wavelengths. Apart from xenon, the *K*-edges of other interesting elements, such as Te, I or the lanthanides, might be used for anomalous-scattering experiments.

The question arises as to whether data collection at very short and ultra-short wavelengths is advantageous if anomalous-scattering effects are not being exploited. Third-generation sources like ESRF, APS and SPRING-8 are clearly capable of delivering intense ultra-short-wavelength undulator radiation, but this is not necessarily true for the lower energy third-generation synchrotrons. This discussion is of particular relevance to the design of proposed national synchrotrons (such as SOLEIL in France and DIAMOND in the UK) because of the extra costs of building facilities that deliver high-energy radiation. Clearly, more case studies will be necessary in order to assess potential benefits and drawbacks of ultra-short wavelengths. We hope that the results of this study will encourage protein crystallographers to move away from the standard 0.9 Å wavelength and to explore the spectral possibilities offered by third-generation synchrotrons more fully.

We would like to thank A. Thompson and V. Biou for useful discussions and C.-I. Brändén for constant support of this project. We also would like to thank one of the referees for his very useful comments.

References

Abrahams, J. P. & Leslie, A. G. W. (1996). *Acta Cryst.* **D52**, 30–42.
Amemiya, Y. (1990). *Synchrotron Rad. News*, **3**, 21–26.
Arndt, U. W. (1984). *J. Appl. Cryst.* **17**, 118–119.
Baker, P. J., Farrants, G. W., Stillman, T. J., Britton, K. L., Helliwell, J. R. & Rice, D. W. (1990). *Acta Cryst.* A**46**, 721–725.
Bourgeois, D., Moy, J.-P., Svensson, S. O. & Kvick, Å. (1994). *J. Appl. Cryst.* **27**, 868–877.
Bourguet, W., Ruff, M., Chambon, P., Gronemeyer, H. & Moras, D. (1995). *Nature (London)*, **375**, 377–382.
Collaborative Computational Project, Number 4 (1994). *Acta Cryst.* D**50**, 760–763.
Colloc'h, N., El Hajji, M., Bachet, B., L'Hermite, G., Schiltz, M., Prangé, T., Castro, B. & Mornon, J. P. (1997). *Nature Struct. Biol.* In the press.
Colloc'h, N., El Hajji, M., Castro, B., Bachet, B., Prangé, T., Schiltz, M. & Mornon, J.-P. (1996). *Acta Cryst.* A**52**, C-96.
Gonzales, A., Denny, R. & Nave, C. (1994). *Acta Cryst.* D**50**, 276–282.
Hammersley, A. P., Brown, K., Burmeister, W., Claustre, L., Gonzales, A., McSweeney, S., Mitchell, E., Moy, J.-P., Svensson, S. O. & Thompson, A. W. (1997). *J. Synchrotron Rad.* **4**, 67–77.
Hammersley, A. P., Svensson, S. O. & Thompson, A. (1994). *Nucl. Instrum. Methods Phys. Res. A*, **346**, 312–321.
Hammersley, A. P., Svensson, S. O., Thompson, A., Graafsma, H., Kvick, Å. & Moy, J.-P. (1995). *Rev. Sci. Instrum.* **66**, 2729–2733.
Helliwell, J. R. (1992). *Macromolecular Crystallography with Synchrotron Radiation.* Cambridge University Press.
Helliwell, J. R., Ealick, S., Doing, P., Irving, T. & Szebenyi, M. (1993). *Acta Cryst.* D**49**, 120–128.
Helliwell, J. R. & Fourme, R. (1983). *The ESRF as a Facility for Protein Crystallography: a Report and Design Study.* CERN, Geneva, Switzerland.
Hubbell, J. H., Veigele, Wm. J., Briggs, E. A., Brown, R. T., Cromer, D. T. & Howerton, R. J. (1975). *J. Phys. Chem. Ref. Data*, **4**, 471–538.
Krause, M. O. & Oliver, J. H. (1979). *J. Phys. Chem. Ref. Data*, **8**, 329–338.
Krauss, N., Schubert, W.-D., Klukas, O., Fromme, P., Witt, H. T. & Saenger, W. (1996). *Nature Struct. Biol.* **3**, 965–973.
Kvick, Å. & Wulff, M. (1992). *Rev. Sci. Instrum.* **63**, 1073–1076.
La Fortelle, E. de & Bricogne, G. (1997). *Methods in Enzymology: Macromolecular Crystallography*, ch. 7, edited by R. M. Sweet & C. W. Carter Jr, pp. 472–494. New York: Academic Press.

Leslie, A. G. W. (1992). In *Joint CCP4 and ESF-EACMB Newsletter on Protein Crystallography*, Vol. 26. SERC Daresbury Laboratory, Warrington WA4 4AD, UK.

Li de la Sierra, I., Pernot, L., Prangé, T., Saludjian, P., Schiltz, M., Fourme, R. & Padrón, G. (1997). *J. Mol. Biol.* **269**, 129–141.

Malashkevich, V. N., Kammerer, R. A., Efimov, V. P., Schulthess, T. & Engel, J. (1996). *Science*, **274**, 761–765.

Matsushita, T. & Hashizume, H. (1983). In *Handbook on Synchrotron Radiation*, Vol. 1, edited by E. Koch. Amsterdam: North Holland.

Meyer, E. F., Radhakrishnan, R., Cole, G. M. & Presta, L. G. (1986). *J. Mol. Biol.* **189**, 553–559.

Moy, J.-P. (1994). *Nucl. Instrum. Methods Phys. Res. A*, **348**, 641–644.

Moy, J.-P., Hammersley, A. P., Svensson, S. O., Thompson, A. W., Brown, K., Claustre, L., Gonzales, A. & McSweeney, S. (1996). *J. Synchrotron Rad.* **3**, 1–5.

Nave, C. (1995). *Rad. Phys. Chem.* **45**, 483–490.

Pernot, L., Li de la Sierra, I., Prangé, T., Saludjian, P., Schiltz, M., Fourme, R. & Padrón, G. (1996). *Acta Cryst.* A**52**, C-222.

Prangé, T., Pernot, L., Colloc'h, N., Longhi, S., Bourguet, W., Fourme, R. & Schlitz, M. (1997). *Proteins Struct. Funct. Genet.* In the press.

Saloman, E. B., Hubbell, J. H. & Scofield, J. H. (1988). *Atom. Data Nucl. Data Tables*, **38**, 1–197.

Sauer, O., Schmidt, A. & Kratky, C. (1997). *J. Appl. Cryst.* **30**, 476–486.

Schiltz, M. (1997). PhD thesis, Université Paris XI Orsay, France.

Schiltz, M., Fourme, R., Broutin, I. & Prangé, T. (1995). *Structure*, **3**, 309–316.

Schiltz, M., Prangé, T. & Fourme, R. (1994). *J. Appl. Cryst.* **27**, 950–960.

Schiltz, M., Shepard, W., Fourme, R., Prangé, T., La Fortelle, E. de & Bricogne, G. (1997). *Acta Cryst.* D**53**, 78–92.

Schindelin, H., Kisker, C., Hilton, J., Rajagopalan, K. V. & Rees, D. C. (1996). *Science*, **272**, 1615–1621.

Schoenborn, B. P. (1965). *Nature (London)*, **208**, 760–762.

Schoenborn, B. P., Watson, H. C. & Kendrew, J. C. (1965). *Nature (London)*, **207**, 28–30.

Stowell, M. H. B., Soltis, S. M., Kisker, C., Peters, J. W., Schindelin, H., Rees, D. C., Cascio, D., Beamer, L., Hart, P. J., Wiener, M. C. & Whitby, F. G. (1996). *J. Appl. Cryst.* **29**, 608–613.

Tilton, R. F., Kuntz, I. D. & Petsko, G. A. (1984). *Biochemistry*, **23**, 2849–2857.

Vitali, J., Robbins, A. H., Almo, S. C. & Tilton, R. F. (1991). *J. Appl. Cryst.* **24**, 931–935.